Magnetic susceptibility of the two-dimensional Hubbard model using a power series for the hopping constant

Alexei Sherman
Institute of Physics, University of Tartu, Riia 142, 51014 Tartu, Estonia

Michael Schreiber
Institut für Physik, Technische Universität, 09107 Chemnitz, Germany
(Received 3 July 2007; published 14 December 2007)

The magnetic susceptibility of the two-dimensional repulsive Hubbard model with nearest-neighbor hopping is investigated using the diagram technique developed for the case of strong correlations. In this technique, a power series in the hopping constant is used. At half-filling, the calculated zero-frequency susceptibility and the square of the site spin reproduce adequately the results of Monte Carlo simulations. Also, in agreement with numerical simulations, no evidence of ferromagnetic correlations was found in the considered range of electron concentrations $0.8 \lesssim \bar{n} \lesssim 1.2$ for the repulsion parameters $8|t| \leqslant U \leqslant 16|t|$. However, for larger $U/|t|$ and $|1-\bar{n}| \approx 0.2$, the nearest-neighbor correlations become ferromagnetic. For $\bar{n} \lesssim 0.94$ and $\bar{n} \gtrsim 1.06$, the imaginary part of the real-frequency susceptibility becomes incommensurate for small frequencies. The incommensurability parameter grows with departure from half-filling and decreases with increasing frequency. This behavior of the susceptibility can explain the observed low-frequency incommensurate response observed in normal-state lanthanum cuprates.

DOI: 10.1103/PhysRevB.76.245112 PACS number(s): 71.10.Fd, 71.27.+a, 75.40.Gb

I. INTRODUCTION

The Hubbard model[1] is thought to be appropriate to describe the main features of electron correlations in narrow energy bands, leading to collective effects such as magnetism and metal-insulator transition. It has been often used to describe real materials exhibiting these phenomena (see, e.g., Refs. 2 and 3, and references therein).

In more than one dimension, the model is not exactly solvable and a variety of numerical and analytical approximate methods were used for its study. Among others, there are Monte Carlo simulations,[4,5] different cluster methods,[6] the composite operator formalism,[7] the generating functional approach,[8] Green's function decoupling schemes,[9] and variational approaches.[10] Along with these methods, various versions of the diagram technique[2,3,11–14] have been used for the investigation of the model. In the case of strong electron correlations, when the ratio of the hopping constant t to the on-site repulsion U is a small parameter, the use of the diagram technique based on the series expansion in this parameter is quite reasonable.

In the present work, we use the diagram technique of Refs. 12 and 14 for investigating the magnetic susceptibility of the one-band two-dimensional repulsive Hubbard model with nearest-neighbor hopping in the case of strong electron correlations. In this version of the diagram technique, terms of the power expansion are expressed through cumulants of creation and annihilation electron operators. The considered model possesses the electron-hole symmetry, and results obtained for electron concentrations $\bar{n} < 1$ are replicated for $\bar{n} > 1$. Therefore, in the following discussion, we shall restrict our consideration to the former region of concentrations.

We found that at half-filling, the calculated temperature dependence of the zero-frequency susceptibility reproduces adequately key features of results of Monte Carlo simulations.[4] The uniform susceptibility tends to a finite value for vanishing temperature. The staggered susceptibility diverges with decreasing temperature, which signals the establishment of the long-range antiferromagnetic order. The transition temperature T_0 is finite, which indicates the violation of the Mermin-Wagner theorem.[15] However, the transition temperature is always lower than the analogous temperature in the random phase approximation (RPA). Besides, the transition temperature decreases by decreasing the ratio $|t|/U$ of the hopping constant and the on-site repulsion, i.e., the violation of the Mermin-Wagner theorem becomes less pronounced on enforcing the condition for which the approximation was developed. For small ratios $|t|/U$, the calculated square of the site spin differs by less than 10% from the data of Monte Carlo simulations. Also, in agreement with Monte Carlo results, we found no evidence of ferromagnetic correlations in the considered range of electron concentrations $0.8 \lesssim \bar{n} \lesssim 1.2$ for the repulsion parameters $8|t| \leqslant U \leqslant 16|t|$. However, for larger $U/|t|$ and $|1-\bar{n}| \approx 0.2$, the nearest-neighbor correlations become ferromagnetic. In the case $U=8|t|$ for $0.94 \lesssim \bar{n} \lesssim 1.06$, the zero-frequency susceptibility and the imaginary part of the susceptibility for low real frequencies are peaked at the antiferromagnetic wave vector (π,π). For smaller and larger concentrations, these susceptibilities become incommensurate—momenta of their maxima deviate from (π,π)—and the incommensurability parameter, i.e., the distance between (π,π) and the wave vector of the susceptibility maximum, grows with departure from half-filling. With increasing frequency, the incommensurability parameter decreases and finally vanishes. This behavior of the strongly correlated system resembles the incommensurate magnetic response observed in the normal-state lanthanum cuprates,[16] and can be used for its explanation.

The main formulas used in the calculations are given in the following section. The discussion of the obtained results

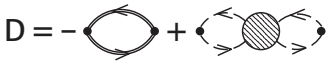

FIG. 1. The diagram equation for $D(\mathbf{k}, i\omega_\nu)$.

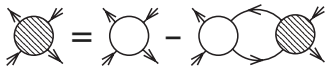

FIG. 2. The Bethe-Salpeter equation for the sum of all four-leg diagrams.

and their comparison with data of Monte Carlo simulations are carried out in Sec. III. Concluding remarks are presented in Sec. IV. The relation between the longitudinal and transversal spin Green's functions is checked in the Appendix.

II. MAIN FORMULAS

The Hubbard model is described by the Hamiltonian

$$H = \sum_{\mathbf{ll}'\sigma} t_{\mathbf{ll}'} a^\dagger_{\mathbf{l}\sigma} a_{\mathbf{l}'\sigma} + \frac{U}{2} \sum_{\mathbf{l}\sigma} n_{\mathbf{l}\sigma} n_{\mathbf{l},-\sigma}, \tag{1}$$

where $a^\dagger_{\mathbf{l}\sigma}$ and $a_{\mathbf{l}\sigma}$ are the electron creation and annihilation operators, respectively, $\mathbf{l}$ labels sites of the square plane lattice, $\sigma = \pm 1$ is the spin projection, $t_{\mathbf{ll}'}$ and U are hopping and on-site repulsion constants, respectively, and $n_{\mathbf{l}\sigma} = a^\dagger_{\mathbf{l}\sigma} a_{\mathbf{l}\sigma}$. Below, we consider the case where only the constant t for hopping between nearest-neighbor sites is nonzero.

In the case of strong correlations, $U \gg |t|$, for calculating Green's functions, it is reasonable to use the expansion in powers of the hopping constant. In the diagram technique of Refs. 12 and 14, this expansion is expressed in terms of site cumulants of electron creation and annihilation operators. We use this technique for calculating the spin Green's function

$$D(\mathbf{l}'\tau', \mathbf{l}\tau) = \langle \mathcal{T} s^\sigma_{\mathbf{l}'}(\tau') s^{-\sigma}_{\mathbf{l}}(\tau) \rangle, \tag{2}$$

where $s^\sigma_{\mathbf{l}} = a^\dagger_{\mathbf{l}\sigma} a_{\mathbf{l},-\sigma}$ is the spin operator, the angular brackets denote the statistical averaging with the Hamiltonian

$$\mathcal{H} = H - \mu \sum_{\mathbf{l}\sigma} n_{\mathbf{l}\sigma},$$

μ is the chemical potential, $\mathcal{T}$ is the time-ordering operator which arranges other operators from right to left in ascending order of times τ, and

$$a_{\mathbf{l}\sigma}(\tau) = \exp(\mathcal{H}\tau) a_{\mathbf{l}\sigma} \exp(-\mathcal{H}\tau).$$

The structure elements of the diagram technique used are site cumulants and hopping constants which connect the cumulants.[12,14] In diagrams, we denote the hopping constants by single directed lines. By using the diagram technique, it can be shown that Green's function (2) satisfies the diagram equation plotted in Fig. 1. In this diagram, after the Fourier transformation over the space and time variables the dual line indicates the full electron Green's function

$$G(\mathbf{k}, n) = -\frac{1}{2} \int_{-\beta}^{\beta} e^{i\omega_n \tau} \langle \mathcal{T} a_{\mathbf{k}}(\tau) a^\dagger_{\mathbf{k}} \rangle d\tau,$$

where $\mathbf{k}$ is the wave vector, the integer n stands for the fermion Matsubara frequency $\omega_n = (2n+1)\pi T$ with the temperature T, and $\beta = T^{-1}$. The shaded circle in Fig. 1 is the sum of all four-leg diagrams, i.e., such diagrams in which starting from any leg one can reach any other leg moving along the hopping lines and cumulants. These diagrams can be separated into reducible and irreducible diagrams. In contrast to the latter, the reducible diagrams can be divided into two disconnected parts by cutting two hopping lines. The sum of all four-leg diagrams satisfies the Bethe-Salpeter equation shown in Fig. 2. Here, the open circle indicates the sum of all irreducible four-leg diagrams. The hopping lines between the open and shaded circles are already renormalized here by the inclusion of all possible irreducible two-leg diagrams into these lines. These irreducible two-leg diagrams cannot be divided into two disconnected parts by cutting one hopping line.[14] As a consequence, the hopping line in Fig. 2 is described by the equation

$$\Theta(\mathbf{k}, n) = t_{\mathbf{k}} + t^2_{\mathbf{k}} G(\mathbf{k}, n), \tag{3}$$

where in the considered model with nearest-neighbor hopping we have $t_{\mathbf{k}} = 2t[\cos(k_x) + \cos(k_y)]$. The irreducible two-leg diagrams can also be inserted in the external lines of the four-leg diagrams in Fig. 1. To mark this renormalization, we use dashed lines in that figure. Each of these lines introduces the multiplier $\Pi(\mathbf{k}, n) = \Theta(\mathbf{k}, n)/t_{\mathbf{k}}$ in the second term on the right-hand side of the equation in Fig. 1. Without the renormalization, this multiplier reduces to unity. As a result, the equations depicted in Figs. 1 and 2 read

$$D(p) = -N^{-1} T \sum_{p_1} G(p_1) G(p + p_1) + N^{-2} T^2 \sum_{p_1 p_2} \Pi(p_1) \times \Pi(p_2) \Pi(p + p_1) \Pi(p + p_2) \Gamma(p_1, p + p_1, p + p_2, p_2), \tag{4}$$

$$\Gamma(p_1, p + p_1, p + p_2, p_2) = \gamma(p_1, p + p_1, p + p_2, p_2) - N^{-1} \times T \sum_{p_3} \gamma(p_1, p + p_1, p + p_3, p_3) \times \Theta(p_3) \Theta(p + p_3) \Gamma(p_3, p + p_3, p + p_2, p_2). \tag{5}$$

Here, the combined indices $p = (\mathbf{k}, i\omega_\nu)$ and $p_j = (\mathbf{k}_j, i\omega_{n_j})$ were introduced, $\omega_\nu = 2\nu\pi T$ is the boson Matsubara frequency, $\Gamma(p_1, p+p_1, p+p_2, p_2)$ is the sum of all four-leg diagrams, $\gamma(p_1, p+p_1, p+p_2, p_2)$ is its irreducible subset, and N is the number of sites.

In the following consideration, we simplify the general equations (4) and (5) by neglecting the irreducible two-leg diagrams in the external and internal lines of the four-leg diagrams and by using the lowest-order irreducible four-leg diagram instead of $\gamma(p_1, p+p_1, p+p_2, p_2)$. This four-leg diagram is described by the second-order cumulant

$$K_2(\tau',\tau,\tau_1',\tau_1) = \langle \mathcal{T}\bar{a}_\sigma(\tau')a_{-\sigma}(\tau)\bar{a}_{-\sigma}(\tau_1')a_\sigma(\tau_1)\rangle_0 + K_1(\tau',\tau_1)K_1(\tau_1',\tau), \quad (6)$$

where the subscript "0" of the angular bracket indicates that the averaging and time dependencies of the operators are determined by the site Hamiltonian

$$H_{\mathbf{l}} = \sum_\sigma [(U/2)n_{\mathbf{l}\sigma}n_{\mathbf{l},-\sigma} - \mu n_{\mathbf{l}\sigma}],$$

$$\bar{a}_{\mathbf{l}\sigma}(\tau) = \exp(H_{\mathbf{l}}\tau)a_{\mathbf{l}\sigma}^\dagger \exp(-H_{\mathbf{l}}\tau),$$

and the first-order cumulant

$$K_1(\tau',\tau) = \langle \mathcal{T}\bar{a}_\sigma(\tau')a_\sigma(\tau)\rangle_0.$$

All operators in the cumulants belong to the same lattice site. Due to the translational symmetry of the problem, the cumulants do not depend on the site index which is, therefore, omitted in the above equations. The expression for K_2 reads

$$\begin{aligned} K_2(n_1,n_1+\nu,n_2+\nu,n_2) = Z^{-1}(&\beta[\delta_{\nu,0}e^{-E_1\beta} + Z^{-1}\delta_{n_1,n_2}(e^{-2E_1\beta} - e^{-(E_0+E_2)\beta})]F(n_1+\nu)F(n_2) \\ &+ e^{-E_0\beta}Ug_{01}(n_1+\nu)g_{01}(n_2)g_{02}(n_1+n_2+\nu)[g_{01}(n_2+\nu)+g_{01}(n_1)] \\ &+ e^{-E_2\beta}Ug_{12}(n_1+\nu)g_{12}(n_2)g_{02}(n_1+n_2+\nu)[g_{12}(n_2+\nu)+g_{12}(n_1)] \\ &- e^{-E_1\beta}\{F(n_1+\nu)g_{01}(n_2)g_{01}(n_2+\nu) + F(n_2)g_{01}(n_1+\nu)g_{01}(n_1) \\ &+ F(n_2)g_{12}(n_2+\nu)[g_{12}(n_1+\nu) - g_{01}(n_1)] + F(n_1+\nu)g_{12}(n_1)[g_{12}(n_2) - g_{01}(n_2+\nu)]\}), \end{aligned} \quad (7)$$

where $E_0=0$, $E_1=-\mu$, and $E_2=U-2\mu$ are the eigenenergies of the site Hamiltonian $H_{\mathbf{l}}$, $Z=e^{-E_0\beta}+2e^{-E_1\beta}+e^{-E_2\beta}$ is the site partition function, $g_{ij}(n)=(i\omega_n+E_i-E_j)^{-1}$, and $F(n)=g_{01}(n)-g_{12}(n)$.

It is worth noting that the used approximation retains the relation

$$D(\mathbf{l}'\tau',\mathbf{l}\tau) = 2D_z(\mathbf{l}'\tau',\mathbf{l}\tau), \quad (8)$$

where

$$D_z(\mathbf{l}'\tau',\mathbf{l}\tau) = \langle \mathcal{T}s_{\mathbf{l}'}^z(\tau')s_{\mathbf{l}}^z(\tau)\rangle \quad (9)$$

and $s_{\mathbf{l}}^z=\frac{1}{2}\Sigma_\sigma \sigma a_{\mathbf{l}\sigma}^\dagger a_{\mathbf{l}\sigma}$ is the z component of spin. Relation (8) follows from the invariance of Hamiltonian (1) with respect to rotations of the spin quantization axis.[17] The proof of Eq. (8) is given in the Appendix.

Equation (7) can be significantly simplified for the case of principal interest $U \gg T$. In this case, if μ satisfies the condition

$$\varepsilon < \mu < U - \varepsilon, \quad (10)$$

where $\varepsilon \gg T$, the exponent $e^{-\beta E_1}$ is much larger than $e^{-\beta E_0}$ and $e^{-\beta E_2}$. Therefore, terms with $e^{-\beta E_0}$ and $e^{-\beta E_2}$ can be omitted in Eq. (7), which gives

$$\begin{aligned} K_2(n_1,n_1+\nu,n_2+\nu,n_2) = \frac{1}{2}\Bigg\{ &\beta\left(\delta_{\nu,0} + \frac{1}{2}\delta_{n_1,n_2}\right)F(n_1+\nu)F(n_2) - F(n_1+\nu)g_{01}(n_2) \\ &\times g_{01}(n_2+\nu) - F(n_2)g_{01}(n_1+\nu)g_{01}(n_1) - F(n_2) \\ &\times g_{12}(n_2+\nu)[g_{12}(n_1+\nu) - g_{01}(n_1)] \\ &- F(n_1+\nu)g_{12}(n_1)[g_{12}(n_2) - g_{01}(n_2+\nu)]\Bigg\}. \end{aligned} \quad (11)$$

From Eq. (5) with the kernel (11), it can be seen that Γ does not depend on momenta $\mathbf{k}_1$ and $\mathbf{k}_2$. Since we neglected irreducible diagrams in the external lines, $\Pi(p)=1$ and, in the second term on the right-hand side of Eq. (4), the summations over $\mathbf{k}_1$, $\mathbf{k}_2$, and n_2 can be carried out instantly. The resulting equation for $\Gamma_{\mathbf{k}}'(\nu,n)=T\Sigma_{n'}\Gamma_{\mathbf{k}}(n,n+\nu,n'+\nu,n')$ reads

$$\begin{aligned} \Gamma_{\mathbf{k}}'(\nu,n) = \frac{1}{2}f_{\mathbf{k}}(\nu,n)\{&2K_2'(\nu,n) + [a_2(-\nu,\nu+n) \\ &- a_1(\nu+n)\beta\delta_{\nu,0}]tt_{\mathbf{k}}y_1(\mathbf{k}\nu) + a_1(\nu+n)tt_{\mathbf{k}}y_2(\mathbf{k}\nu) \\ &+ a_4(-\nu,\nu+n)tt_{\mathbf{k}}y_3(\mathbf{k}\nu) + a_3(-\nu,\nu+n)tt_{\mathbf{k}}y_4(\mathbf{k}\nu)\}, \end{aligned} \quad (12)$$

where

$$\begin{aligned} K_2'(\nu,n) &= T\sum_{n'} K_2(n,n+\nu,n'+\nu,n') \\ &= \frac{1}{2}\left\{\left[\beta\delta_{\nu,0} + \frac{1}{2}a_1(n)\right]a_1(n+\nu) - a_2(-\nu,n+\nu) + \frac{1}{U-i\omega_\nu}a_4(-\nu,n+\nu) + a_3(-\nu,n+\nu)\right\}, \end{aligned} \quad (13)$$

$$\begin{aligned} f_{\mathbf{k}}(\nu,n) &= \left[1 + \frac{1}{4}F(n)F(\nu+n)tt_{\mathbf{k}}\right]^{-1}, \\ y_i(\mathbf{k}\nu) &= T\sum_n a_i(\nu,n)\Gamma_{\mathbf{k}}'(\nu,n), \\ a_1(n) &= F(n), \quad a_2(\nu,n) = g_{01}(n)g_{01}(\nu+n), \\ a_3(\nu,n) &= F(n)g_{12}(\nu+n), \quad a_4(\nu,n) = g_{12}(n) - g_{01}(\nu+n). \end{aligned} \quad (14)$$

Multiplying Eq. (12) by $a_i(\nu,n)$ and summing over n, we obtain a system of four linear algebraic equations for y_i,

$$y_i = b_i + (c_{i2} - c_{i1}\beta\delta_{\nu,0})y_1 + c_{i1}y_2 + c_{i4}y_3 + c_{i3}y_4, \quad (15)$$

where

$$b_i = T\sum_n a_i(\nu,n)K_2'(\nu,n)f_{\mathbf{k}}(\nu,n),$$

$$c_{ij} = tt_{\mathbf{k}}\frac{T}{2}\sum_n a_i(\nu,n)a_j(-\nu,\nu+n)f_{\mathbf{k}}(\nu,n).$$

System (15) can easily be solved. Thus, in the used approximation, the Bethe-Salpeter equation (5) can be solved exactly. In notations (14), the second term on the right-hand side of Eq. (4) can be rewritten as

$$\left(\frac{T}{N}\right)^2\sum_{p_1p_2}\Gamma = \frac{T}{2}\Bigg\{[\beta\delta_{\nu,0}(1-tt_{\mathbf{k}}y_1)+tt_{\mathbf{k}}y_2] \times\sum_n f_{\mathbf{k}}(\nu,n)a_1(n+\nu) + \frac{1}{2}\sum_n f_{\mathbf{k}}(\nu,n)a_1(n)a_1(n+\nu) - (1-tt_{\mathbf{k}}y_1)\sum_n f_{\mathbf{k}}(\nu,n)a_2(-\nu,n+\nu) + \left(tt_{\mathbf{k}}y_3+\frac{1}{U-i\omega_\nu}\right)\sum_n f_{\mathbf{k}}(\nu,n)a_4(-\nu,n+\nu) + (1+tt_{\mathbf{k}}y_4)\sum_n f_{\mathbf{k}}(\nu,n)a_3(-\nu,n+\nu)\Bigg\}. \quad (16)$$

In subsequent calculations, we shall use the Hubbard-I approximation[1] for the electron Green's function in the first term on the right-hand side of Eq. (4). In the used diagram technique, this approximation is obtained if in the Larkin equation the sum of all irreducible two-leg diagrams is substituted by the first-order cumulant.[12,14] Provided that condition (10) is fulfilled, the electron Green's function in the Hubbard-I approximation reads

$$G(\mathbf{k}n) = \frac{i\omega_n+\mu-U/2}{(i\omega_n+\mu)(i\omega_n+\mu-U)-t_{\mathbf{k}}(i\omega_n+\mu-U/2)}. \quad (17)$$

III. MAGNETIC SUSCEPTIBILITY

From the Lehmann representation,[18] it can be shown that $D_z(\mathbf{k}\nu)$ has to be real, non-negative,

$$D_z(\mathbf{k}\nu) \geqslant 0 \quad (18)$$

and symmetric, $D_z(\mathbf{k}\nu)=D_z(\mathbf{k},-\nu)$. In view of Eq. (8), analogous relations are fulfilled for $D(\mathbf{k}\nu)$. However, we found that condition (18) is violated for $\nu=0$ and some momentum if the temperature drops below some critical value T_0, which depends on the ratio $|t|/U$ and on μ. As the temperature T_0 is approached from above, $D(\mathbf{k},0)$ tends to infinity, which leads to the establishment of long-range spin correlations. Therefore, like in the RPA,[18,19] we interpret this behavior of Green's function as a transition to a long-range order. Near half-filling, the highest temperature T_0 occurs for the antiferromagnetic momentum (π,π). Thus, near half-filling, the system exhibits transition to the state with the long-range antiferromagnetic order.

In our calculations, T_0 is finite. Since we consider the two-dimensional model and the broken symmetry is continuous, this result is in contradiction to the Mermin-Wagner theorem[15] and shows that the used approximation somewhat overestimates the effect of the interaction. However, it is worth noting that the value of T_0 decreases with decreasing ratio $|t|/U$, i.e., the violation of the Mermin-Wagner theorem becomes less pronounced on enforcing the condition for which the approximation was developed. Notice that other approximate methods, including RPA[4] and cluster methods,[6] lead also to the violation of the Mermin-Wagner theorem. In the following calculations, we consider only the region $T > T_0$.

It was also found that for $\nu\neq 0$, condition (18) is violated in a small area of the Brillouin zone near the Γ point. Green's function is small for such momenta, and small negative values of $D(\mathbf{k}\nu)$ here are a consequence of the used approximations. It is worth noting that the renormalization of internal and external hopping lines should improve the behavior of $D(\mathbf{k}\nu)$ in this region.

To check the used approximation, we shall compare our calculated results with data of Monte Carlo simulations[4] on the temperature dependence of the zero-frequency susceptibility at half-filling and on the square of the site spin $\langle\mathbf{S}^2\rangle$. In the usual definition,[18] the susceptibility $\chi(\mathbf{k}\nu)$ differs from $D(\mathbf{k}\nu)$ only in a constant multiplier. For convenience, in comparison with results of Ref. 4 in this work, we set

$$\chi(\mathbf{k}\nu) = D(\mathbf{k}\nu). \quad (19)$$

The square of the site spin is given by the relation

$$\langle\mathbf{S}^2\rangle = \frac{3}{2}\frac{T}{N}\sum_{\mathbf{k}\nu} D(\mathbf{k}\nu), \quad (20)$$

where Eq. (8) is taken into account.

The calculated zero-frequency magnetic susceptibility for $\mathbf{k}=0$ and half-filling is shown in Fig. 3. Results obtained in Monte Carlo simulations[4] and in the RPA are also shown here for comparison. The RPA results are described by the equations[18]

$$\chi_{\mathrm{RPA}}(\mathbf{k}) = \frac{2\chi_0(\mathbf{k})}{1-U\chi_0(\mathbf{k})},$$

$$\chi_0(\mathbf{k}) = -\frac{1}{N}\sum_{\mathbf{k}'}\frac{f(t_{\mathbf{k}'}-\mu)-f(t_{\mathbf{k}'+\mathbf{k}}-\mu)}{t_{\mathbf{k}'}-t_{\mathbf{k}'+\mathbf{k}}}, \quad (21)$$

where $f(E)=[\exp(E\beta)+1]^{-1}$. Notice that to use the same scale for the susceptibility as in Ref. 4, our calculated values (19) in Figs. 3 and 4 were multiplied by the factor 2. Also, it should be mentioned that for $T>2|t|=U/2$, we violate con-

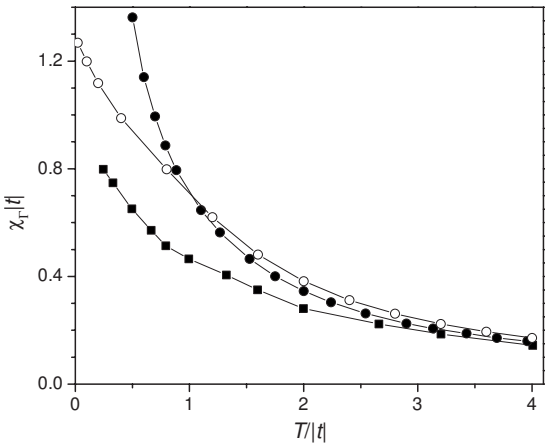

FIG. 3. The zero-frequency magnetic susceptibility at $\mathbf{k}=0$ vs temperature at half-filling and $t=-U/4$. Filled squares and filled and open circles are results of the Monte Carlo simulations (Ref. 4), random phase approximation, and our calculations, respectively.

dition (10); however, the calculated high-temperature susceptibility is in reasonable agreement with the Monte Carlo data. It deserves attention that in contrast to the RPA susceptibility which diverges for low temperatures, the susceptibility in our approach tends to a finite value as it must.

The staggered magnetic susceptibility χ_M is shown in Fig. 4. As mentioned above, in the used approximation, as the temperature approaches T_0 from above, χ_M tends to infinity, which signals the establishment of the long-range antiferromagnetic order. For parameters of Fig. 4, $T_0 \approx 0.64|t|$. The transition temperature T_0 is finite; however, for the considered range of parameters $4|t| \leqslant U \leqslant 16|t|$, it is always lower than the respective temperature in the RPA. Accordingly, our calculated values of χ_M in Fig. 4 are closer to the Monte Carlo data than the RPA results.

The temperature variation of the square of the site spin [Eq. (20)] is shown in Fig. 5 together with the data of Monte

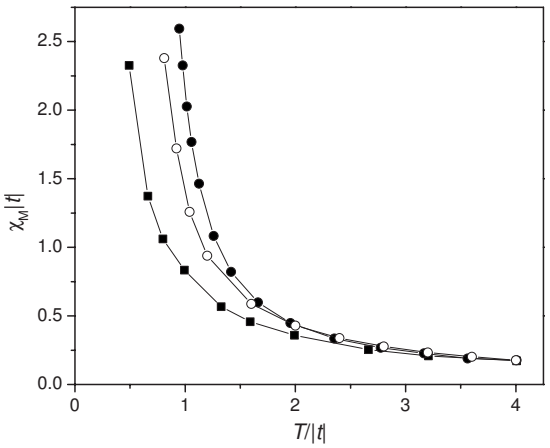

FIG. 4. The zero-frequency magnetic susceptibility at $\mathbf{k}=(\pi,\pi)$ vs temperature at half-filling and $t=-U/4$. Filled squares and filled and open circles are results of the Monte Carlo simulations (Ref. 4), random phase approximation, and our calculations, respectively.

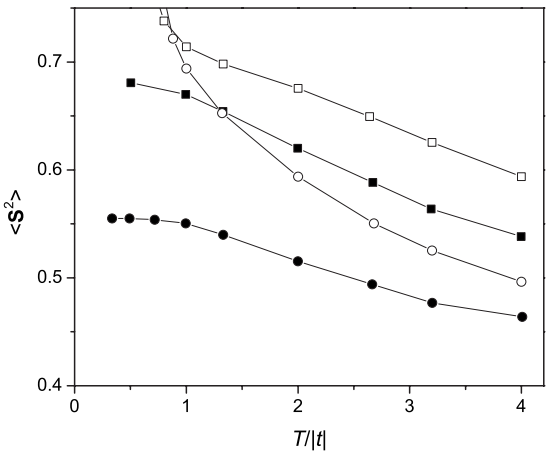

FIG. 5. The square of the site spin $\langle \mathbf{S}^2 \rangle$ vs temperature at half-filling. Filled symbols are data of Monte Carlo simulations (Ref. 4); open symbols are our results. Squares and circles correspond to the cases $t=-U/8$ and $t=-U/4$, respectively.

Carlo simulations.[4] As might be expected, the results for the smaller ratio $|t|/U$ more closely reproduce the data of numerical simulations. For $t=-U/8$, our calculations replicate the Monte Carlo data for $T \gtrsim |t|$, and the difference between the two series of results is less than 10%. This difference is at least partly connected with the simplification made above when irreducible two-leg diagrams were dropped from internal and external lines of the four-leg diagrams. The difference becomes even smaller if, in accord with the Mermin-Wagner theorem, T_0 is set as the zero of the temperature scale and our calculated curve is offset by this temperature to the left. On approaching T_0, our approximation becomes inapplicable for calculating $\langle \mathbf{S}^2 \rangle$—it starts to grow rapidly and exceeds the maximum value $\frac{3}{4}$.

The concentration dependence of $\langle \mathbf{S}^2 \rangle$ near half-filling is shown in Fig. 6. The range of the electron concentration $\bar{n}=\Sigma_\sigma \langle n_{\mathbf{l}\sigma} \rangle$, which corresponds to the chemical potential shown in this figure, spans approximately 0.8–1.2 for $t=-U/8$. As would be expected, $\langle \mathbf{S}^2 \rangle$ decreases rapidly with departure from half-filling.

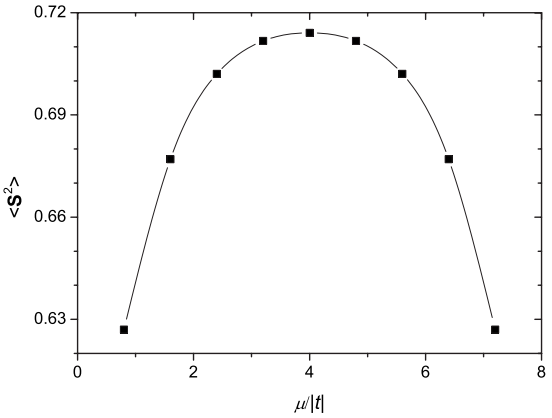

FIG. 6. The square of the site spin $\langle \mathbf{S}^2 \rangle$ vs the chemical potential for $t=-U/8$ and $T=|t|$.

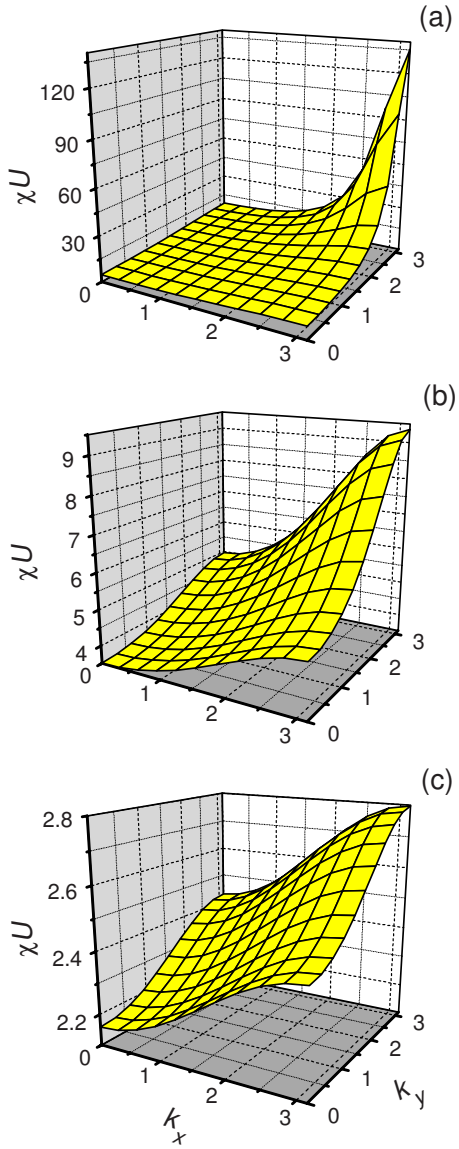

FIG. 7. (Color online) The zero-frequency magnetic susceptibility at half-filling for $t=-U/8$ in a quadrant of the Brillouin zone. (a) $T=0.06U$, (b) $T=0.1U$, and (c) $T=0.2U$.

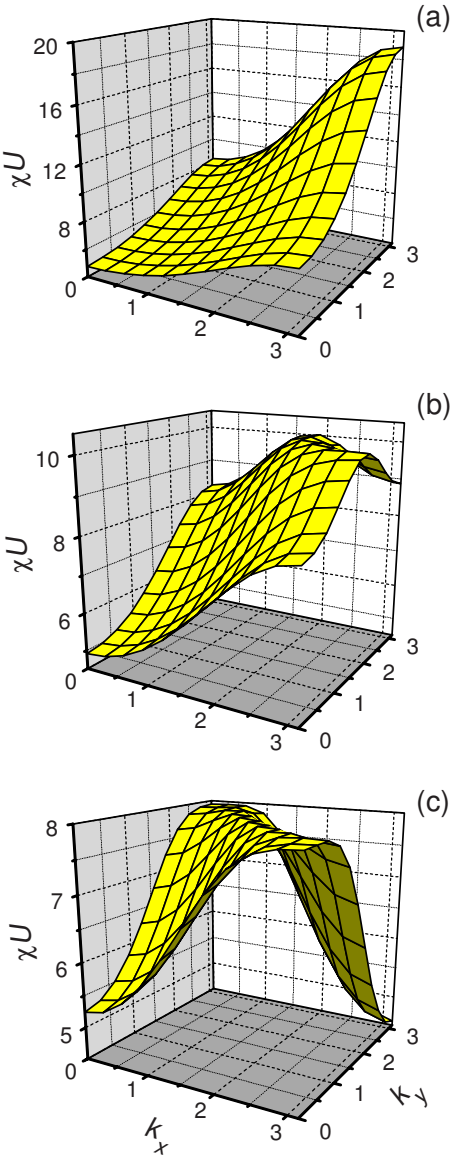

FIG. 8. (Color online) The zero-frequency magnetic susceptibility for $t=-U/8$ and $T=0.06U$ in a quadrant of the Brillouin zone. (a) $\mu=0.2U$, (b) $\mu=0.15U$, and (c) $\mu=0.1U$.

The momentum dependence of the zero-frequency susceptibility at half-filling and its variation with temperature are shown in Fig. 7. At half-filling, the susceptibility is peaked at the antiferromagnetic wave vector (π,π). For temperatures which are only slightly higher than T_0, the peak intensity is large [Fig. 7(a)], which leads to a slow decrease of spin correlations with distance and long correlation lengths (see below). With increasing temperature, the peak intensity of the susceptibility decreases rapidly [Figs. 7(b) and 7(c)], which results in a substantial reduction of the correlation length. In this case, for distances of several lattice periods, the spin correlations are small; nevertheless, they remain antiferromagnetic.

The situation is changed with departure from half-filling. The zero-frequency susceptibility for different electron concentrations is shown in Fig. 8. The values of the concentration which correspond to Figs. 8(a), 8(b), and 8(c) are $\bar{n}\approx 0.94$, 0.88, and 0.81, respectively. Notice the rapid decrease of the peak intensity of the susceptibility with doping [cf. Figs. 8(a) and 7(a)]. Starting from $\bar{n}\approx 0.94$, the susceptibility becomes incommensurate—the maximum value of the susceptibility is not located at (π,π)—and the incommensurability parameter, i.e., the distance between (π,π) and the wave vector of the susceptibility maximum, grows with departure from half-filling. It is interesting to notice that for $\bar{n}<1$, the zero-frequency susceptibility diverges when the temperature approaches some critical temperature in the same manner as it does at half-filling. For $t=-U/8$ and $0.94\leqslant\bar{n}\leqslant 1$, the divergence first occurs at (π,π), while for smaller electron concentrations, it appears at incommensurate wave vectors. For $\bar{n}<1$, the value of the critical temperature is less than T_0—the temperature at which the transition to the long-range order occurs at half-filling. The

critical temperature decreases with decreasing $\bar{n}$. If, in accord with the Mermin-Wagner theorem, we identify T_0 with zero temperature, we have to conclude that for $\bar{n}<1$, the system undergoes a virtual transition at negative temperatures, while for $T \geqslant 0$, it is governed by short-range order. In view of the particle-hole symmetry, analogous conclusions can be made for $\bar{n}>1$.

By analyzing equations of the previous section, it can be seen that the momentum dependence of the zero-frequency susceptibility is mainly determined by the multiplier $y_1(\mathbf{k}, \nu=0)$ in the first term on the right-hand side of Eq. (16). At half-filling, the susceptibility is commensurate, since this term is peaked at (π, π) and diverges at this momentum when $T \to +T_0$, as the determinant of the system (15) vanishes. At departure from half-filling, the behavior of y_1 is governed by the term b_1 in this system. The term contains the sum

$$T\sum_n a_1^2(0,n) f_{\mathbf{k}}(0,n) = T\sum_n F^2(n)\left[1 + \frac{1}{4} t t_{\mathbf{k}} F^2(n)\right]^{-1}, \tag{22}$$

where $F(n) = -U[(i\omega_n + \mu)(i\omega_n + \mu - U)]^{-1}$. For half-filling, the sum has a maximum at (π, π); however, with departure from half-filling, the maximum shifts from (π, π) and the susceptibility becomes incommensurate.

Together with the zero-frequency susceptibility, the imaginary part of the real-frequency susceptibility,

$$\chi''(\mathbf{k}\omega) = \mathrm{Im}\, D(\mathbf{k}, \omega + i\eta), \quad \eta \to +0, \tag{23}$$

becomes also incommensurate. This quantity is of special interest, because it determines the dynamic structure factor measured in neutron scattering experiments.[20] To carry out the analytic continuation of $D(\mathbf{k}\nu)$ to the real-frequency axis, an algorithm[21] based on the use of Padé approximants can be applied. In this calculation, 300 values of $D(\mathbf{k}\nu)$ at equally spaced imaginary frequencies in the upper half-plane were used. The obtained dependencies of the susceptibility on the momentum for a fixed transfer frequency ω and the dispersion of low-frequency maxima in χ'' are shown in Fig. 9. The susceptibility is shown in the first Brillouin zone and can be extended to the second zone by reflection with respect to the right y axis. As seen from Figs. 9(a) and 9(b), with departure from half-filling, $\chi''(\mathbf{k}\omega)$ becomes incommensurate and the incommensurability parameter grows with increasing $1-\bar{n}$.

This behavior of the susceptibility $\chi''(\mathbf{k}\omega)$ in the Hubbard model resembles the low-frequency incommensurate magnetic response observed by inelastic neutron scattering in lanthanum cuprates.[16] In these crystals, the incommensurability is observed both in the normal and superconducting states. For small transfer frequencies ω, the maxima of the susceptibility are located on the edge of the Brillouin zone. For the parameters of Fig. 9(a), our calculated susceptibility is also peaked on the zone edge. However, for other parameters, the susceptibility on the diagonal may be comparable to that on the zone edge. This uncertainty in the position of the susceptibility maxima may be connected to errors introduced in the calculation results by the procedure of analytic continuation to real frequencies.

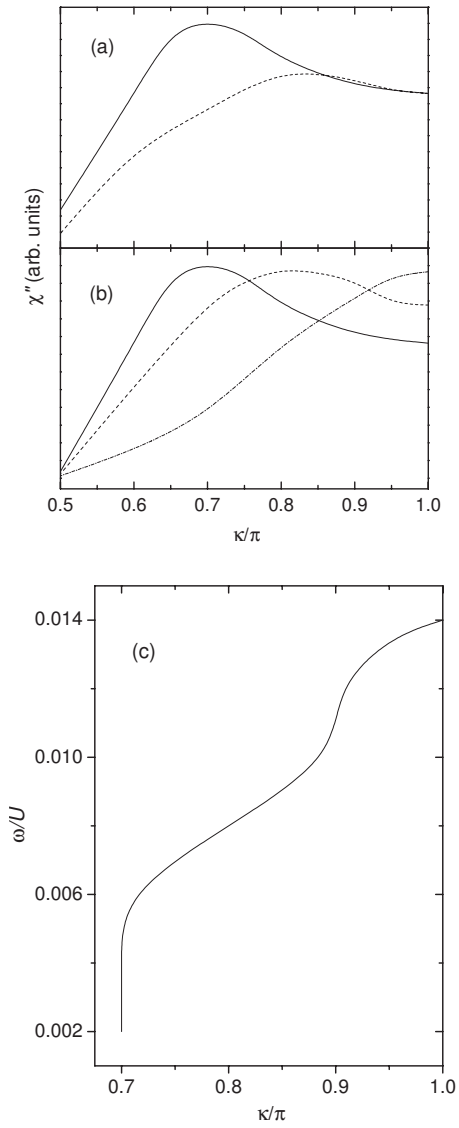

FIG. 9. (a) The momentum dependence of $\chi''(\mathbf{k}\omega)$ along the edge [solid line, $\mathbf{k}=(\pi, \kappa)$] and diagonal [dashed line, $\mathbf{k}=(\kappa, \kappa)$] of the Brillouin zone for $t=-0.11U$, $\omega=0.002U$, and $\bar{n} \approx 0.88$. (b) The momentum dependence of $\chi''(\mathbf{k}\omega)$ along the zone edge for $\bar{n} \approx 0.88$ (solid line), $\bar{n} \approx 0.94$ (dashed line), and $\bar{n}=1$ (dash-dotted line). $t=-0.11U$ and $\omega=0.002U$. (c) The dispersion of maxima in $\chi''(\mathbf{k}\omega)$ along the zone edge for $t=-0.11U$ and $\bar{n} \approx 0.88$.

In experiment, for small ω, the incommensurability parameter grows with the hole concentration $1-\bar{n}$ in the range $0.04 \lesssim 1-\bar{n} \lesssim 0.12$ and saturates for larger values. This behavior of the incommensurability parameter is reproduced in our calculations [see Fig. 9(b)] and its values are close to those observed experimentally. For a fixed hole concentration, the incommensurability parameter decreases with increasing ω and, at some frequency ω_r, the incommensurability disappears and the susceptibility $\chi''(\mathbf{k}\omega)$ appears to be peaked at the antiferromagnetic momentum.[22] The same behavior is observed in the Hubbard model [see Fig. 9(c)]. In

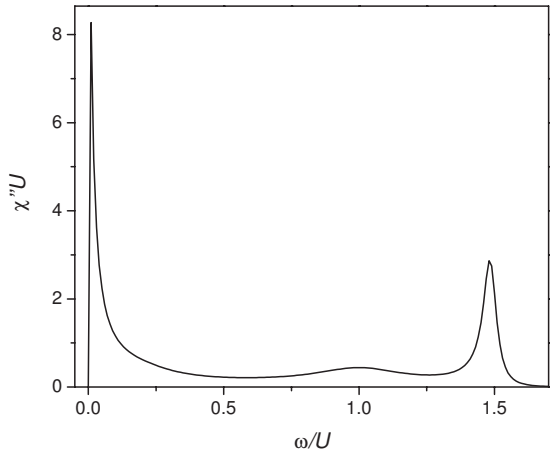

FIG. 10. The susceptibility $\chi''(\mathbf{k}\omega)$ for $\mathbf{k}=(\pi,\pi)$, $t=-U/8$, $T=0.06U$, and $\mu=0.2U$ ($\bar{n}\approx 0.94$).

lanthanum cuprates for the hole concentrations $1-\bar{n}\approx 0.12$, the frequency $\omega_r \approx 50$ meV. In Fig. 9(c), we chose parameters so that ω_r is close to this value (for the superexchange constant $J=4t^2/U\approx 0.15$ eV and $t=-0.11U$, we find $U=3.1$ eV, $t=0.34$ eV, and $\omega_r=44$ meV). Notice that like in experiment, ω_r decreases with decreasing $1-\bar{n}$.

A similar incommensurability is observed in $YBa_2Cu_3O_{7-y}$ (Ref. 23); however, in this case, due to a larger superconducting temperature and gap, the magnetic incommensurability is usually observed in the superconducting state and the low-frequency part of the susceptibility is suppressed. As follows from the above discussion, in the Hubbard model, the magnetic incommensurability is a property of strong electron correlations. The similarity of the mentioned experimental and calculated results gives ground to consider these strong correlations as a possible mechanism of the low-frequency incommensurability observed in experiment. A similar mechanism was observed for the related t-J model in Ref. 24.

In experiment,[22,23] for frequencies $\omega > \omega_r$, the susceptibility $\chi''(\mathbf{k}\omega)$ becomes again incommensurate such that the dispersion of maxima in $\chi''(\mathbf{k}\omega)$ resembles a sandglass. The most frequently used interpretations of this dispersion are based on the picture of itinerant electrons with the susceptibility calculated in the RPA[25] and on the stripe picture.[22,26] In Ref. 24, the sandglass dispersion was obtained in the t-J model in the regime of strong electron correlations without the supposition of the existence of stripes. In this latter work, the part of the sandglass dispersion for $\omega > \omega_r$ was related to the dispersion of excitations of localized spins. A similar notion was earlier suggested in Ref. 27. In our present calculations, we did not obtain this upper part of the dispersion, since the used approximation does not describe the appearance of localized spins. A typical example of the frequency dependence of the susceptibility $\chi''(\mathbf{k}\omega)$, which up to the multiplier π^{-1} coincides with the spin spectral function, is shown in Fig. 10. The susceptibility usually contains several maxima, one of which is located at $\omega \ll U$, while others are placed at frequencies of the order of U. Since the localized spin excitations have frequencies in the range $0 \leqslant \omega \lesssim 2J$,

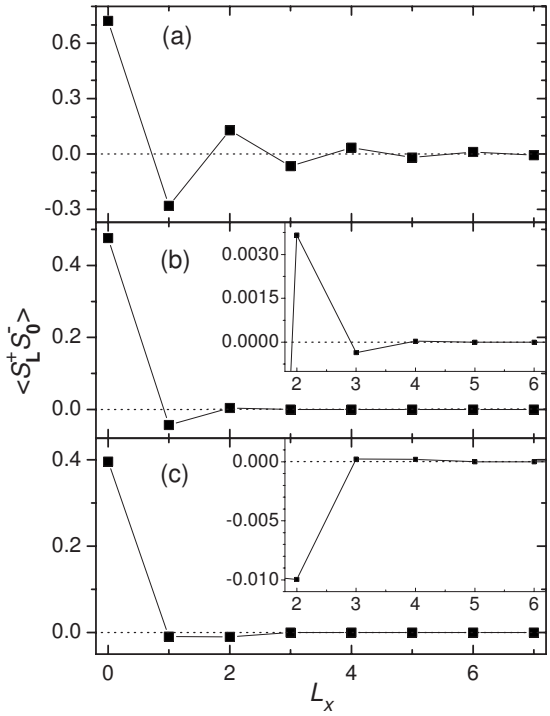

FIG. 11. The spin-spin correlator $\langle s_{\mathbf{L}}^+ s_{\mathbf{0}}^- \rangle$ for $\mathbf{L}=(L_x,0)$ and $t=-U/8$. (a) $T=0.06U$, $\mu=0.5U$; (b) $T=0.125U$, $\mu=0.5U$; and (c) $T=0.06U$, $\mu=0.1U$ ($\bar{n}\approx 0.81$). Insets in (b) and (c) demonstrate the same data as in the main plots in a larger scale.

where $J=4t^2/U \ll U$, the former maximum could be taken as a signal for such excitation. However, the intensity of the maximum usually grows with temperature and with departure from half-filling. This indicates that the maximum is more likely due to a bound electron-hole state in which both components belong to the same Hubbard subband, while in the high-frequency maxima, the components belong to different subbands.

In connection with the Nagaoka theorem,[28] it is of interest to investigate the tendency toward the establishment of the ferromagnetic ordering with departure from half-filling. For a finite U, this problem was investigated by different analytical methods[4,19,29,30] and by Monte Carlo simulations.[4] Our results for the spin-spin correlator,

$$\langle s_{\mathbf{L}}^+ s_{\mathbf{0}}^- \rangle = \frac{T}{N} \sum_{\mathbf{k}\nu} \cos(\mathbf{kL}) D(\mathbf{k}\nu), \tag{24}$$

as a function of the distance L_x between spins are shown in Fig. 11 for different parameters. Figure 11(a) demonstrates the short-range antiferromagnetic order at half-filling for a temperature which is slightly above T_0 (as discussed above in connection with Fig. 5, for such temperatures, the value of $\langle s_{\mathbf{0}}^+ s_{\mathbf{0}}^- \rangle$ is somewhat overestimated by the used approximation). Figure 11(b) corresponds also to half-filling to somewhat higher temperature. In this case, the correlations are still antiferromagnetic though they are characterized by a correlation length which is much shorter than that in Fig. 11(a). We have found that the correlation length diverges when $T \to T_0$, which indicates the transition to the long-range

antiferromagnetic order. Similar weak antiferromagnetic correlations were also obtained for moderate departures from half-filling. Figure 11(c) corresponds to the lowest filling $\bar{n} \approx 0.81$ which is allowed by condition (10) for the given ratio $U/|t|$. According to the mean-field theory[4] and the generalized RPA[19] in this case the system has a ferromagnetic ground state. As seen from Fig. 11(c), our calculated spin-spin correlations are still antiferromagnetic even for nearest-neighbor spins. This result is in agreement with Monte Carlo simulations[4] carried out for the same parameters. Analogous result was also obtained for $U=16|t|$. However, a tendency for the establishment of ferromagnetic correlations can also be seen from the comparison of Figs. 11(a) and 11(c)—the antiferromagnetic spin correlation on nearest-neighbor sites becomes smaller with doping. For larger ratios of $U/|t|$, we can ascertain that the correlation changes sign and becomes ferromagnetic. In particular, it happens at $U/|t|=25$ and $\bar{n} \approx 0.77$. For these parameters, condition (10) is still fulfilled.

IV. CONCLUDING REMARKS

In this paper, we investigated the magnetic susceptibility of the two-dimensional repulsive Hubbard model using the diagram technique developed for the case of strong electron correlations. In this technique, the power series in the hopping constant is used. At half-filling, the calculated temperature dependence of the zero-frequency susceptibility reproduces adequately key features of results of Monte Carlo simulations. The uniform susceptibility tends to a finite value for vanishing temperature. The staggered susceptibility diverges with decreasing temperature, which signals the establishment of the long-range antiferromagnetic order. The transition temperature is finite, which indicates the violation of the Mermin-Wagner theorem. However, the transition temperature is always lower than the analogous temperature in the RPA. Besides, the transition temperature decreases with the decrease of the ratio $|t|/U$ of the hopping constant and the on-site repulsion, i.e., the violation of the Mermin-Wagner theorem becomes less pronounced on enforcing the condition for which the approximation was developed. For small ratios $|t|/U$, the calculated square of the site spin differs by less than 10% from the data of Monte Carlo simulations. Also, in agreement with Monte Carlo results, we found no evidence of ferromagnetic correlations in the considered range of electron concentrations $0.8 \lesssim \bar{n} \lesssim 1.2$ for the repulsion parameters $8|t| \leqslant U \leqslant 16|t|$. However, for larger $U/|t|$ and $|1-\bar{n}| \approx 0.2$, the nearest-neighbor correlations become ferromagnetic. In the case $U=8|t|$ for $0.94 \lesssim \bar{n} \lesssim 1.06$, the zero-frequency susceptibility and the imaginary part of the susceptibility for low real frequencies are peaked at the antiferromagnetic wave vector (π,π). For smaller and larger concentrations, these susceptibilities become incommensurate—momenta of their maxima are shifted from (π,π)—and the incommensurability parameter, i.e., the distance between (π,π) and the momentum of the maximum susceptibility, grows with departure from half-filling. With increasing transfer frequency, the incommensurability parameter decreases and finally vanishes. This behavior of the susceptibility in the strongly correlated system can explain the observed low-frequency incommensurate response in the normal state of lanthanum cuprates.

ACKNOWLEDGMENTS

This work was partially supported by the ETF Grant No. 6918 and by the DFG.

APPENDIX

In this Appendix, we prove the symmetry relation (8). In the zeroth order of the perturbation expansion for Green's function (9), we find

$$\begin{aligned} D_z^{(0)}(\mathbf{l}'\tau',\mathbf{l}\tau) &= \frac{1}{4}\sum_{\sigma\sigma'} \sigma\sigma'[K_2'(\tau'\sigma',\tau'\sigma',\tau\sigma,\tau\sigma)\delta_{\mathbf{ll}'} \\ &\quad + K_1(\tau'\tau')K_1(\tau\tau) - K_1(\tau'\tau)K_1(\tau\tau')\delta_{\mathbf{ll}'}\delta_{\sigma\sigma'}] \\ &= \frac{1}{2}\delta_{\mathbf{ll}'}[K_2'(\tau'\sigma,\tau'\sigma,\tau\sigma,\tau\sigma) - K_2'(\tau'\sigma;\tau'\sigma;\tau, \\ &\quad - \sigma;\tau,-\sigma) - K_1(\tau'\tau)K_1(\tau\tau')], \end{aligned} \tag{A1}$$

where we took into account that the first-order cumulant $K_1(\tau'\tau)$ does not depend on σ and, therefore, the second term in the sum vanishes. Up to the multiplier $\frac{1}{2}$, the last term on the right-hand side of Eq. (A1) coincides with the respective term in the expansion for Green's function (2). In the used diagram technique, K_1 describes the bare electron Green's function. Therefore, that term contributes to the electron bubble shown in Fig. 1. From the higher-order terms, it can be seen that the inclusion of irreducible two-leg diagrams into the two bare Green's functions of that term retains the one-to-one correspondence between terms of the bubble diagrams in D and D_z, and the additional multiplier $\frac{1}{2}$ in the terms of D_z.

The second-order cumulant K_2' in Eq. (A1) is defined as

$$\begin{aligned} K_2'(\tau'\sigma,\tau\sigma,\tau_1'\sigma_1,\tau_1\sigma_1) &= \langle \mathcal{T}\bar{a}_\sigma(\tau')a_\sigma(\tau)\bar{a}_{\sigma_1}(\tau_1')a_{\sigma_1}(\tau_1)\rangle \\ &\quad - K_1(\tau',\tau)K_1(\tau_1',\tau_1) \\ &\quad + K_1(\tau',\tau_1)K_1(\tau_1',\tau)\delta_{\sigma\sigma_1}. \end{aligned} \tag{A2}$$

This definition is more general than Eq. (6)—the latter is obtained from Eq. (A2) if we set $\sigma_1=-\sigma$ and interchange annihilation operators in K_2. After the Fourier transformation, we find

$$K_2'(n_1\sigma;n_1+\nu,\sigma;n_2+\nu,\sigma_1;n_2\sigma_1) = Z^{-1}(\beta[(\delta_{\nu 0}\delta_{\sigma\sigma_1}-\delta_{n_1 n_2})e^{-E_1\beta}+Z^{-1}(\delta_{\nu 0}-\delta_{n_1 n_2}\delta_{\sigma\sigma_1})(e^{-(E_0+E_2)\beta}-e^{-2E_1\beta})]F(n_1+\nu)F(n_2)$$
$$-\delta_{\sigma,-\sigma_1}e^{-E_0\beta}Ug_{01}(n_1+\nu)g_{01}(n_2)g_{02}(n_1+n_2+\nu)[g_{01}(n_2+\nu)+g_{01}(n_1)]$$
$$-\delta_{\sigma,-\sigma_1}e^{-E_2\beta}Ug_{12}(n_1+\nu)g_{12}(n_2)g_{02}(n_1+n_2+\nu)[g_{12}(n_2+\nu)+g_{12}(n_1)]+\delta_{\sigma,-\sigma_1}e^{-E_1\beta}\{F(n_1$$
$$+\nu)g_{01}(n_2)g_{01}(n_2+\nu)+F(n_2)g_{01}(n_1+\nu)g_{01}(n_1)+F(n_2)g_{12}(n_2+\nu)[g_{12}(n_1+\nu)-g_{01}(n_1)]$$
$$+F(n_1+\nu)g_{12}(n_1)[g_{12}(n_2)-g_{01}(n_2+\nu)]\}), \tag{A3}$$

where the notations are the same as in Eq. (7). From these two equations, it can be seen that

$$K_2(n_1,n_1+\nu,n_2+\nu,n_2) = K_2'(n_1\sigma;n_1+\nu,\sigma;n_2+\nu,\sigma;n_2\sigma) - K_2'(n_1\sigma;n_1+\nu,\sigma;n_2+\nu,-\sigma;n_2,-\sigma) \tag{A4}$$

and the analogous equation is fulfilled for the Fourier-transformed quantities. Thus, zeroth-order terms in the expansions for D and D_z coincide up to the factor $\frac{1}{2}$.

The next terms in the considered expansions for D and D_z contain two second-order cumulants and appear in the second order. These terms read

$$D^{(2)}(\mathbf{l}'\tau',\mathbf{l}\tau) = -\int\int_0^\beta d\tau_1 d\tau_2 t_{\mathbf{l}\mathbf{l}'}t_{\mathbf{l}'\mathbf{l}}K_2(\tau',\tau',\tau_1,\tau_2)K_2(\tau_2,\tau_1,\tau,\tau), \tag{A5}$$

$$D_z^{(2)}(\mathbf{l}'\tau',\mathbf{l}\tau) = -\frac{1}{4}\sum_{\sigma\sigma'\sigma_1}\int\int_0^\beta d\tau_1 d\tau_2 t_{\mathbf{l}\mathbf{l}'}t_{\mathbf{l}'\mathbf{l}} \times K_2'(\tau'\sigma',\tau'\sigma',\tau_1\sigma_1,\tau_2\sigma_1) \times K_2'(\tau_2\sigma_1,\tau_1\sigma_1,\tau\sigma,\tau\sigma). \tag{A6}$$

Using twice relation (A4) in Eq. (A6), one can see that $D^{(2)}=2D_z^{(2)}$. Analogous equations for higher-order terms can be proven in the same manner. Thus, relation (8) is fulfilled.

[1] J. Hubbard, Proc. R. Soc. London, Ser. A **276**, 238 (1963); M. C. Gutzwiller, Phys. Rev. Lett. **10**, 159 (1963); J. Kanamori, Prog. Theor. Phys. **30**, 275 (1963).

[2] Yu. A. Izyumov and Yu. N. Skryabin, *Statistical Mechanics of Magnetically Ordered Systems* (Consultants Bureau, New York, 1988).

[3] S. G. Ovchinnikov and V. V. Valkov, *Hubbard Operators in the Theory of Strongly Correlated Electrons* (Imperial College Press, London, 2004).

[4] J. E. Hirsch, Phys. Rev. B **31**, 4403 (1985).

[5] A. Moreo, S. Haas, A. W. Sandvik, and E. Dagotto, Phys. Rev. B **51**, 12045 (1995); C. Gröber, R. Eder, and W. Hanke, *ibid.* **62**, 4336 (2000).

[6] T. Maier, M. Jarrell, T. Pruschke, and M. H. Hettler, Rev. Mod. Phys. **77**, 1027 (2005); M. Aichhorn, E. Arrigoni, M. Potthoff, and W. Hanke, Phys. Rev. B **74**, 024508 (2006); A.-M. S. Tremblay, B. Kyung, and D. Sénéchal, Fiz. Nizk. Temp. **32**, 561 (2006).

[7] F. Mancini and A. Avella, Adv. Phys. **53**, 537 (2004).

[8] Yu. A. Izyumov, N. I. Chaschin, D. S. Alexeev, and F. Mancini, Eur. Phys. J. B **45**, 69 (2005).

[9] V. Yu. Irkhin and A. V. Zarubin, Phys. Rev. B **70**, 035116 (2004).

[10] G. Seibold, F. Becca, P. Rubin, and J. Lorenzana, Phys. Rev. B **69**, 155113 (2004).

[11] R. O. Zaitsev, Zh. Eksp. Teor. Fiz. **70**, 1100 (1976) [Sov. Phys. JETP **43**, 574 (1976)].

[12] M. I. Vladimir and V. A. Moskalenko, Teor. Mat. Fiz. **82**, 428 (1990) [Theor. Math. Phys. **82**, 301 (1990)]; W. Metzner, Phys. Rev. B **43**, 8549 (1991).

[13] S. Pairault, D. Sénéchal, and A.-M. S. Tremblay, Eur. Phys. J. B **16**, 85 (2000).

[14] A. Sherman, Phys. Rev. B **73**, 155105 (2006); **74**, 035104 (2006).

[15] N. D. Mermin and H. Wagner, Phys. Rev. Lett. **17**, 1133 (1966).

[16] T. E. Mason, G. Aeppli, S. M. Hayden, A. P. Ramirez, and H. A. Mook, Phys. Rev. Lett. **71**, 919 (1993); K. Yamada, C. H. Lee, K. Kurahashi, J. Wada, S. Wakimoto, S. Ueki, H. Kimura, Y. Endoh, S. Hosoya, G. Shirane, R. J. Birgeneau, M. Greven, M. A. Kastner, and Y. J. Kim, Phys. Rev. B **57**, 6165 (1998).

[17] E. Fradkin, *Field Theories of Condensed Matter Systems* (Addison-Wesley, New York, 1991).

[18] G. D. Mahan, *Many-Particle Physics* (Plenum, New York, 1981).

[19] Yu. A. Izyumov and B. M. Letfulov, J. Phys.: Condens. Matter **2**, 8905 (1990); Yu. A. Izyumov, B. M. Letfulov, and E. V. Shipitsyn, *ibid.* **4**, 9955 (1992); **6**, 5137 (1994).

[20] M. A. Kastner, R. J. Birgeneau, G. Shirane, and Y. Endoh, Rev. Mod. Phys. **70**, 897 (1998).

[21] H. J. Vidberg and J. W. Serene, J. Low Temp. Phys. **29**, 179 (1977); G. A. Baker, Jr. and P. Graves-Morris, *Padé Approximants* (Addison-Wesley, London, 1981).

[22] J. M. Tranquada, H. Woo, T. G. Perring, H. Goka, G. D. Gu, G. Xu, M. Fujita, and K. Yamada, Nature (London) **429**, 534 (2004).

[23] M. Arai, T. Nishijima, Y. Endoh, T. Egami, S. Tajima, K. To-

mimoto, Y. Shiohara, M. Takahashi, A. Garrett, and S. M. Bennington, Phys. Rev. Lett. **83**, 608 (1999).
[24] A. Sherman and M. Schreiber, Int. J. Mod. Phys. B **19**, 2145 (2005); **21**, 669 (2007).
[25] D. Z. Liu, Y. Zha, and K. Levin, Phys. Rev. Lett. **75**, 4130 (1995); J. Brinckmann and P. A. Lee, *ibid.* **82**, 2915 (1999); M. R. Norman, Phys. Rev. B **61**, 14751 (2000).
[26] M. Vojta, T. Vojta, and R. K. Kaul, Phys. Rev. Lett. **97**, 097001 (2006); G. Seibold and J. Lorenzana, Phys. Rev. B **73**, 144515 (2006).
[27] V. Barzykin and D. Pines, Phys. Rev. B **52**, 13585 (1995).
[28] Y. Nagaoka, Phys. Rev. **147**, 392 (1966).
[29] D. Penn, Phys. Rev. **142**, 350 (1966).
[30] K. Kubo, Prog. Theor. Phys. **64**, 758 (1980).